Journal of Power Sources 195 (2010) 6709–6718

Contents lists available at ScienceDirect

Journal of Power Sources

journal homepage: www.elsevier.com/locate/jpowsour

On the synthesis and performance of flame-made nanoscale $La_{0.6}Sr_{0.4}CoO_{3-\delta}$ and its influence on the application as an intermediate temperature solid oxide fuel cell cathode

Andre Heel*, Peter Holtappels, Thomas Graule

EMPA, Swiss Federal Laboratories for Materials Testing and Research, Laboratory for High Performance Ceramics, Ueberlandstrasse 129, CH-8600 Duebendorf, Switzerland

ARTICLE INFO

Article history:
Received 24 December 2009
Received in revised form 11 March 2010
Accepted 5 April 2010
Available online 13 April 2010

Keywords:
$La_{0.6}Sr_{0.4}CoO_{3-\delta}$ (LSC)
Cathode
Nanoparticle
Flame spray synthesis
Electrolyte interaction
CO_2 sensitivity

ABSTRACT

Flame spray synthesis (FSS), a large-scale powder processing technique is used to prepare nanoscale $La_{0.6}Sr_{0.4}CoO_{3-\delta}$ powder for solid oxide fuel cell cathodes from water-based nitrate solutions. Influence of processing is investigated on basis of the as-synthesised powders by X-ray powder diffraction (XRD), thermal gravimetric analysis (TGA), nitrogen adsorption (BET) and electron microscopy (SEM and TEM).

Against the background of a nanostructured cathode morphology for an intermediate temperature solid oxide fuel cell (IT-SOFC) at 600 °C, an optimised and high surface area flame-made $La_{0.6}Sr_{0.4}CoO_{3-\delta}$ nanopowder of 29 $m^2\,g^{-1}$ is used to investigate its performance and chemical reaction with common electrolytes ($Y_{0.16}Zr_{0.84}O_{2-\delta}$, $Ce_{0.9}Gd_{0.1}O_{2-\delta}$ and $Sc_{0.20}Ce_{0.01}Zr_{0.79}O_{2-\delta}$). Secondary phase analysis from XRD measurements revealed a substantially lower $La_2Zr_2O_7$ and $SrZrO_3$ formation in comparison to conventional spray pyrolysed and submicron powder of about 9 $m^2\,g^{-1}$. TGA and resistivity measurements proofed that $La_{0.6}Sr_{0.4}CoO_{3-\delta}$ is non-sensitive towards carbonate formation under CO_2 containing atmospheres. Electronic bulk conductivity of 2680 S cm^{-1} (600 °C) and 3340 S cm^{-1} (500 °C) were measured in air and as function of oxygen partial pressure (2×10^5 Pa > $p(O_2)$ > 1.2×10^{-2} Pa) in the temperature range between 400 and 900 °C. Electrochemical performance is determined by impedance spectroscopy on symmetrical cells of screen printed nanoscale $La_{0.6}Sr_{0.4}CoO_{3-\delta}$ on $Ce_{0.9}Gd_{0.1}O_{2-\delta}$ substrates from which an area specific resistance (ASR) of 0.96 Ω cm^2 at 600 °C and 0.14 Ω cm^2 at 700 °C were obtained.

1. Introduction

The research field of solid oxide fuel cells (SOFCs) is challenging with the reduction of the operating temperature from 800 to 1000 °C down to 550–750 °C [1,2]. This so-called intermediate or low temperature concept of a solid oxide fuel cell (IT-SOFC) will increase the long-term durability of such a system by avoiding strong temperature induced degradation phenomena, e.g. cathode–electrolyte interdiffusion and formation of non-conductive blocking compositions. It offers also the possibility to reduce costs by implementation of inexpensive materials for housing components, interconnectors, sealing, etc. due to the reduction of the thermal degradation.

The problem of increased resistance of the electrolyte at lower temperatures can be addressed by a reduction of electrolyte thickness or by alternative materials with a higher ionic conductivity. However, a reduction of the operating temperature of a SOFC system increases also polarization losses associated with the electrode. To overcome this drawback, several strategies are conceivable: outgoing from a cathode optimisation, the development of new compositions or application of mixed ionic-electronic conductors (MIEC) and that in combination with a microstructure optimisation is the most promising one and would improve the performance at intermediate temperatures significantly. The application of a MIEC, and here especially compositions among the series of $La_{1-x}Sr_xCoO_{3-\delta}$ outperform most other materials by their ionic-electronic conductivity [3–5] and this in combination with a high catalytic activity regarding oxygen reduction [6,7]. Since several research activities have shown an enhanced performance of nanocrystalline microstructures [8,9], it can be expected that cathode structures made from ultra-fine particles or nanopowders can minimize the polarization losses of the cathode layer when applied in an intermediate temperature SOFC. High number of grain boundaries as well as the high surface area could enhance oxygen diffusion [10,11]. The synthesis of nanocrystalline MIEC's have been demonstrated by different techniques such as sol–gel [8], glycine–nitrate [12], impregnation [13], pulsed laser deposition [14] or RF sputtering [15]. Low material output or economic reasons restrict the transfer to industrial cell production. On the other hand spray pyrolysis or solid state reactions have to deal with time consuming and expensive annealing and wet grinding steps to reach a fine graded powder, where nanocrystallinity is difficult

* Corresponding author. Tel.: +41 44 823 4199; fax: +41 44 823 4150.
E-mail address: andre.heel@empa.ch (A. Heel).

0378-7753/$ – see front matter © 2010 Elsevier B.V. All rights reserved.
doi:10.1016/j.jpowsour.2010.04.006

to achieve or impossible to conserve during the initial preparation steps at elevated temperatures.

This work is focusing on the flame spray synthesis (FSS) of nanoscale $La_{0.6}Sr_{0.4}CoO_{3-\delta}$ (LSC) at application relevant output (up to 400 g h^{-1}) and at highly demanded economically production costs by usage of low-cost processing techniques and materials [16,17]. The aim of this work was set on the production and optimisation of nanocrystalline powders with high specific surface area (SSA) and its application as a nanostructured $La_{0.6}Sr_{0.4}CoO_{3-\delta}$ cathode in an SOFC technology at intermediate temperatures of about 600 °C. A comprehensive report is given here about the unique material properties of such high temperature derived nanopowders and how this affects its application. Particle size, morphology, phase purity and composition, as well as reaction and secondary phase formation towards common and relevant electrolyte compositions are investigated. Furthermore, material properties like bulk conductivity, $p(O_2)$ dependency or electrochemical performance in terms of ASR are determined and CO_2 sensitivity is evaluated against the background of the synthesis route and derived particle size.

2. Experimental

2.1. Flame spray setup

The $La_{0.6}Sr_{0.4}CoO_{3-\delta}$ powders were produced by a special flame spray synthesis technique (FSS). A detailed technical description is given elsewhere and considerable differences from conventional plants are explained especially in terms of usage of aqueous solutions [17]. In brief, a liquid precursor mixture is atomised into a fine droplet aerosol via a variable oxygen flow (0.3–1.0 l s^{-1}, 99.95%) and axially sprayed into an acetylene/oxygen premixed flame (0.217 l s^{-1} C_2H_2, 99.6% and 0.283 l s^{-1} O_2, 99.5%, both Carbagas, Switzerland). Representative samples up to 2 g are collected by sampling aerosol via a bypass on glass fibre filters. The main aerosol is collected in a semi-industrial pulse-jet baghouse with an active filtration area of 3.5 m^2 (FFR 6/1.5, Friedli AG, Switzerland).

2.2. Precursor system

Precursor solutions were prepared by dissolving stoichiometric amounts of lanthanum(III) nitrate hexahydrate (99.99%, Auer Remy, Germany), strontium(II) nitrate (≥99.0%, Fluka, Switzerland) and cobalt(III) nitrate hexahydrate (99.9%, Auer Remy, Germany) in a proper solvent. Mixture of deionised water (H_2O) and acetic acid ($C_2H_4O_2$, 99%, Sigma–Aldrich, Switzerland) was used as solvent in different water–fuel-ratios. Acetic acid was used due its low price, harmlessness and relatively high solubility of nitrates in such a mixture. Stoichiometric cation amounts of La:Sr:Co (6:4:10) were added sequentially as the corresponding nitrates into the solvent mixture under stirring. As standard condition a precursor solution concentration of 0.75 mol l^{-1} was adjusted for the $La_{0.6}Sr_{0.4}CoO_{3-\delta}$ synthesis.

2.3. Cathode powder characterisation

Crystal structure and secondary phase formation was analysed by X-ray diffraction (PANalytical X'Pert Pro MPD, Netherlands) with Cu K_α radiation (λ = 1.540598 Å). Analyses were carried out over a 2θ range of 20–80° with a step size of 0.0167°. Crystallite size was determined by Scherrer equation [18,19]:

$$d_{XRD} = \frac{K\lambda}{\beta \cos\theta} \quad (1)$$

where K is a constant shape factor and β is the full-width-at-half-maximum value (FWHM) at the corresponding Bragg angle. Cathode–electrolyte reaction tests were carried out on pellets, consisting of 1:1 weight ratio of $La_{0.6}Sr_{0.4}CoO_{3-\delta}$ and of the corresponding electrolyte powder. Pellets with a diameter of 15 mm were uniaxially pressed (29 MPa) to get an intimate contact and were fired either for 125 h at 800 °C or for 4 h at 1000 °C. Quantitative phase analyses were carried out by Rietveld analysis implemented in X'Pert Highscore (PANalytical, Netherlands).

Conventional $La_{0.6}Sr_{0.4}CoO_{3-\delta}$ materials were synthesised as reference by spray pyrolysis (SP) of the corresponding nitrates and annealed for 24 h at 1050 °C to get phase pure $La_{0.6}Sr_{0.4}CoO_{3-\delta}$. From subsequent high energy, liquid-based planetary ball milling, a powder with a specific surface area of 9 m^2 g^{-1} was obtained. As electrolyte composition either $Y_{0.16}Zr_{0.84}O_{2-\delta}$ (YSZ, SSA = 16 m^2 g^{-1}, TZ-8Y, Tosoh, Japan), $Ce_{0.9}Gd_{0.1}O_{2-\delta}$ (CGO, SSA = 8 m^2 g^{-1}, H.C. Starck, Germany) or $Sc_{0.20}Ce_{0.01}Zr_{0.79}O_{2-\delta}$ (ScCeZ, SSA = 17 m^2 g^{-1} [16]) were applied.

Specific surface area (SSA) was determined from a five-point nitrogen adsorption isotherm at 77 K by applying Brunauer–Emmett–Teller theory (BET). All powders were first dried at 180 °C for 3 h in a nitrogen flow and afterwards measured on a SA 3100 (Coulter Electronics, USA). The BET-equivalent particle diameter can be calculated by assuming monodisperse, spherical and non-aggregated particles:

$$d_{BET} = \frac{6}{\rho SSA} \quad (2)$$

where ρ is the density of the corresponding phase pure composition and SSA the specific surface area.

Particles were collected directly from the flame on a carbon coated copper TEM grid by a pneumatic assisted particle sampling system (University of Duisburg, Germany). Afterwards, particle morphology and composition were investigated by HR-TEM (Philips CM30, 300 kV, Netherlands).

Shrinkage behaviour of the as-synthesised powders and the thermal expansion coefficient (TEC) of sintered sample bars were determined by dilatometry in environmental air with heating and cooling rates of 5 K min^{-1} (Baehr Thermoanalyse DIL 802, Germany).

CO_2 sensitivity and decomposition behaviour were investigated by thermal gravimetric analysis (STA 409 CD thermobalance, Netzsch, Germany) with heating and cooling rates of 1 K min^{-1} up to 900 °C in synthetic air or CO_2 containing synthetic air (≥99.99%, Carbagas, Switzerland).

For the resistivity measurements between 25 and 900 °C a four-point DC setup with data acquisition system (Keithley Instruments 2750, Germany) was used. $La_{0.6}Sr_{0.4}CoO_{3-\delta}$ nanopowders were uniaxially pressed and sintered at 1200 °C to reach a density above 95% with a dimension of 55 mm × 3.9 mm × 0.75 mm. Atmosphere was adjusted by a variable flow of N_2, Ar, O_2 and CO_2 (all ≥99.95%, Carbagas, Switzerland) regulated by mass-flow-controller (Voegtlin Instruments, Switzerland). The oxygen content of the atmosphere was recorded at the gas inlet of the furnace via a Rapidox 2100 oxygen analyser (Cambridge Sensotec Limited, United Kingdom). Electrochemical impedance spectroscopy (EIS) was carried out on screen printed symmetrical cells out of flame-made, nanoscale $La_{0.6}Sr_{0.4}CoO_{3-\delta}$ (platinum | $La_{0.6}Sr_{0.4}CoO_{3-\delta}$ | $Ce_{0.9}Gd_{0.1}O_{2-\delta}$ | $La_{0.6}Sr_{0.4}CoO_{3-\delta}$ | platinum) with an active electrode area of 10 mm × 10 mm placed in a Probostat unit (NorECs, Norway) in environmental air. A frequency response analyser (Solartron 1260, Ametek, UK) was used at frequencies of 10^6 to 10^{-1} Hz with a polarization potential of 10 mV. Electrochemical data were obtained by decreasing the sample temperature in 50 °C steps and actually after a 1 h time period to allow sample equilibration: afterwards impedance spectra were collected during an acquisition time of 4 h at which stable performance was observed.

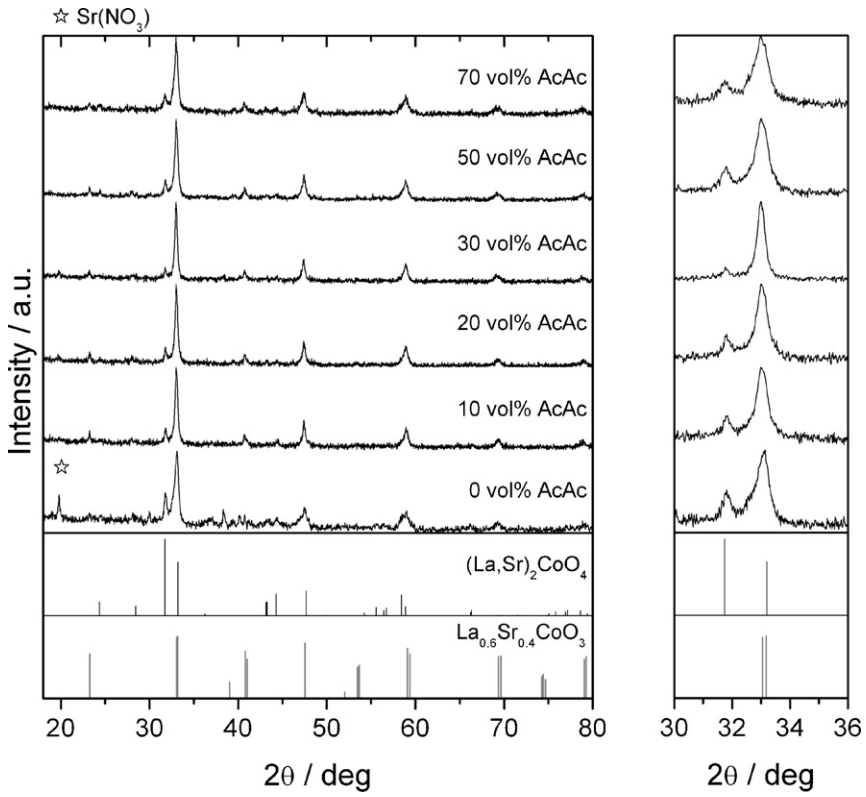

Fig. 1. Diffraction pattern of as-synthesised $La_{0.6}Sr_{0.4}CoO_{3-\delta}$ powders as function of the combustible acetic acid fraction (0–70 vol.%) and magnification of the $2\theta = 30–36^{\circ}$ range. $La_{0.6}Sr_{0.4}CoO_3$ (PDF code 01-089-5719) and $(La,Sr)_2CoO_4$ (PDF code 01-83-2411) are indicated by peak position and intensity as reference at the bottom.

3. Results

3.1. Powder synthesis

Powder quality in terms of homogeneity and phase purity but also particle size distribution and specific surface area strongly depend on the synthesis condition. Here it was the author's intention to focus on large-scale production of cost efficient but nanoscale powder. Because of the later cathode powders processing as screen printing pastes, the specific surface area was strictly limited to a maximum of $40\,m^2\,g^{-1}$. Powders with higher SSA are critical to stabilise and this can be counterproductive, due to the resulting paste viscosity and the solid loading of the paste, but this is described elsewhere in detail [20]. With the following parameters, i.e. precursor concentration of $0.75\,mol\,l^{-1}$ and precursor flow of $20\,ml\,min^{-1}$, a powder production rate of $135\,g\,h^{-1}$ was established.

Powder production via flame spray synthesis (FSS) in dependence of the acetic acid to water ratio in Fig. 1 revealed, that already nitrates in pure water or 0 vol.% acetic acid (AcAc) resulted mainly in the desired $La_{0.6}Sr_{0.4}CoO_{3-\delta}$ phase (PDF code 01-089-5719) [21]. However, a secondary phase was observed, which was identified as $(La,Sr)_2CoO_4$ (PDF code 01-83-2411) [22]. From a deconvolution of XRD spectra and quantitative phase analysis a 27 wt% fraction of $(La,Sr)_2CoO_4$ was determined. This amount of secondary phase depends strongly on the combustible fraction of the solvent mixture (Fig. 2). Pure water is cooling down the flame and inhibits a homogeneous mixing of the elements on an atomic level in the particles. Furthermore, the single nitrates possess a different solubility in the solvent, what leads to a precipitation at the sprayed droplet surface during its evaporation [23]. The interested readers refer to a previous study on flame-made $La_{0.6}Sr_{0.4}Co_{0.2}Fe_{0.8}O_3$ and $Ba_{0.5}Sr_{0.5}Co_{0.8}Fe_{0.2}O_3$ nanopowders [17].

Powders obtained from a flame synthesis with an increasing fraction of 0 up to 70 vol.% of acetic acid showed in first instance gradually finer particles with higher SSA and secondly a minimum in the formation of $(La,Sr)_2CoO_4$. The higher the acetic acid fraction, the more combustion enthalpy is provided to the flame reactor and the more the aerosol gets diluted by the decomposition of acetic acid into gaseous H_2O and CO_2. Both effects resulted in a linear increase of the SSA from $12\,m^2\,g^{-1}$ (80 nm) up to $36\,m^2\,g^{-1}$ (26 nm) as well as in a particle morphology with better homogeneity. The large irregular shaped and several microns large particles are reduced and spherical, crystalline, nanoscale particles are dominating (Fig. 3). But it

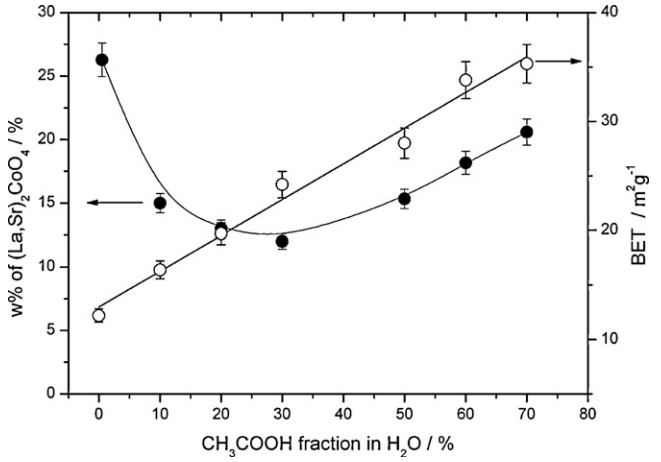

Fig. 2. Mass of secondary $(La,Sr)_2CoO_4$ phase in the as-prepared $La_{0.6}Sr_{0.4}CoO_{3-\delta}$ powders as function of the combustible acetic acid fraction (●) and the corresponding BET (○).

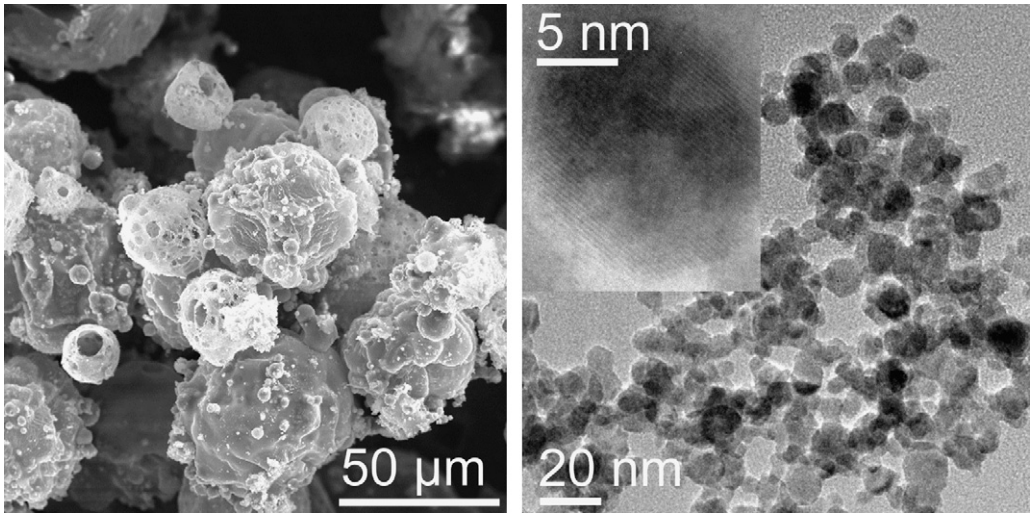

Fig. 3. Comparison of flame-made $La_{0.6}Sr_{0.4}CoO_{3-\delta}$ powders derived from nitrates in different solvent mixtures. Micron-sized, porous and core–shell structured powder morphology from pure water (left). Homogenous, spherical and nanoscale particles from 30 wt% of acetic acid in water (right). The reader may pay attention to the different magnification (50 μm vs. 20 nm). Inset shows high resolution magnification of crystalline nanoparticles.

has to be mentioned, that still a bimodal particle size distribution was obtained and a fraction of about 10 vol.% of the powder consists of massive, spherical particles in the range of 50–200 nm.

The increased energy transfer from the larger fractions of combustible acetic acid into the flame had also a positive effect on the secondary phase formation and optimal condition was found at ~30 vol.% of acetic acid in water, where the amount of $(La,Sr)_2CoO_4$ was reduced from 27 wt% down to 12 wt% (Fig. 2). A moderate increase of $(La,Sr)_2CoO_4$ was observed again for higher fractions of acetic acid, probably due to an enhanced cobalt evaporation and the subsequent secondary phase formation under progressively harsher flame conditions: higher flame temperatures and longer residence times in the flame due to an enlargement of the flame height by the larger amounts of combustible substances. However, here the cobalt precipitates again on the already formed nanoparticles by a so-called heterogeneous condensation process during the flame synthesis or more precisely during the cooling phase [24]. Such an evaporation of cobalt is common and well known in powder processing and needs a precise control over synthesis conditions. But in a former study we have already shown on several cobalt containing nanopowders like $La_{0.6}Sr_{0.4}Co_{0.2}Fe_{0.8}O_3$ or $Ba_{0.5}Sr_{0.5}Co_{0.8}Fe_{0.2}O_3$ via elemental analysis by inductively coupled plasma optical emission spectroscopy (ICP-OES), that the assumed and desired cobalt content is present and is not lost [17]. As a conclusion of these observations, we assume that this cobalt oxide is probably in an amorphous state. It is proofed in the following Section 3.2 about phase formation, that there is no cobalt missing, since the expected unit cell parameter are derived by additional firing.

TGA measurements of the as-prepared nanopowders in dry synthetic air confirmed that a certain fraction of combustible solvent is indispensable to guarantee enhanced precursor decomposition (Fig. 4). Starting from nitrates in pure water, an overall mass loss of 17.0 wt% was measured. With an increasing acetic acid fraction this mass loss could be significantly reduced. The mass losses are caused by undecomposed residues and were reduced down to 11.3 and 5.2 wt% for 10 and 30 vol.% of acetic acid in the solvent mixture. Higher acetic acid fractions did not result in any further reduction. All powders in the as-prepared condition showed an initial mass loss from room temperature up to 180 °C by physisorbed water. Afterwards a progressive and solvent fraction depending mass loss up to 750 °C took place, which origins from several overlapping decomposition steps of intermediates, i.e. nitrate decomposition, loss of crystal water, etc. Between 750 and 900 °C a further minor mass loss of about 0.1 wt% is caused by the temperature driven change in the oxygen non-stoichiometry δ in $La_{0.6}Sr_{0.4}CoO_{3-\delta}$, as it is typical for such perovskite materials by compensation of valence state changes. Change of δ takes place over the whole temperature range (see Section 3.5 about CO_2 sensitivity), but due to the superposition with the precursor caused mass loss, it gets only obvious in the high temperature range. However, the less acetic acid, the more core–shell, hollow and porous particles are formed by precipitating nitrates [23,25]. The resulting large mass loss can be explained by such porous or hollow particle morphology, in which the precursors are partially enclosed and survived the flame spray process (Fig. 3, left). But with increasing acetic acid amounts, droplets get disrupted more effectively by the acetic acid combustion and the liquid-to-gas transfer is less hindered. As a result a more homogeneous nanoscale powder is produced (Fig. 3, right).

For all investigations in the following sections, powder from a production with 30 vol.% content of acetic acid and therefore the lowest amount of $(La,Sr)_2CoO_4$ were used. The desired specific surface area and hence the particle size was adjusted by choosing processing parameter as given in the beginning of this section.

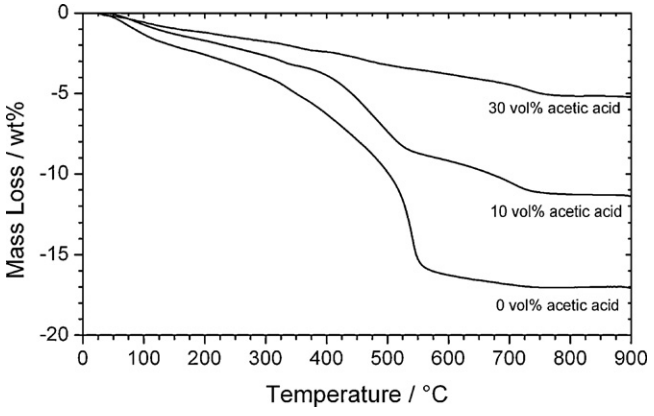

Fig. 4. TGA analyses of as-prepared $La_{0.6}Sr_{0.4}CoO_{3-\delta}$ nanopowders for a varying acetic acid fraction (0, 10 and 30 vol.%) in water.

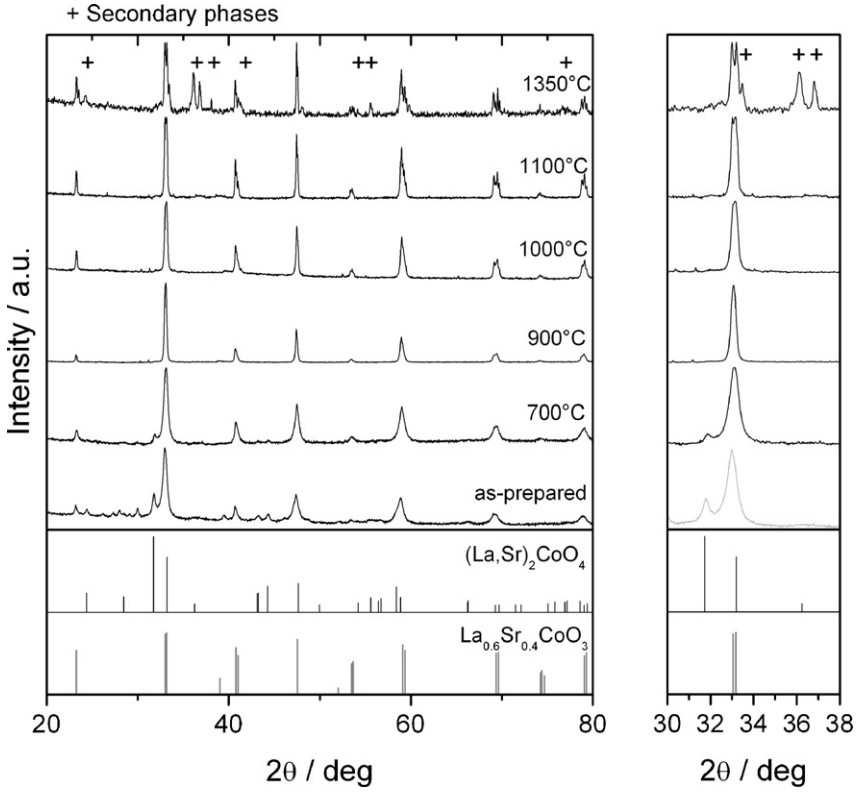

Fig. 5. Diffraction pattern of as-prepared $La_{0.6}Sr_{0.4}CoO_{3-\delta}$ powder, and after thermal treatment at 700, 900, 1000, 1100 and 1350 °C. A magnification of the representative $2\theta = 31–35°$ range is given on the right hand side. $La_{0.6}Sr_{0.4}CoO_3$ and $(La,Sr)_2CoO_4$ references are indicated by peak position and intensity at the bottom.

3.2. Phase formation and powder morphology

As-synthesised $La_{0.6}Sr_{0.4}CoO_{3-\delta}$ powders derived from the most-favoured conditions were treated in air for 3 h at various temperatures between 700 and 1350 °C to investigate the crystalline phase evolution, change of particle size and morphology. Already the powder in the as-synthesised state showed strong reflections from crystalline phases, but crystallinity gets further improved with thermal treatment at 700 and 900 °C. In parallel the XRD patterns indicate the formation of single phase $La_{0.6}Sr_{0.4}CoO_{3-\delta}$ perovskite at 900 °C and reflections attributed to $(La,Sr)_2CoO_4$ are below the detection limit (Fig. 5). Higher temperatures of 1000 and 1100 °C did not affect the phase composition and only further peak narrowing by crystal growth is observed. But different secondary phases appeared at 1350 °C, which clearly indicate the progressive decomposition of the desired phase. Evaporated cobalt formed distinct blue cobalt oxide precipitations on the powder substrate and free cobalt oxide was identified by XRD, as well as needle like precipitations were observed by SEM (not shown here).

Influence of the thermal treatment on the flame-made powder morphology and grain size evolution is determined from suspended and dried powder layers (Fig. 6). For the as-synthesised powders an initial average grain size of 17 nm was determined by XRD from peak broadening analyses and Scherrer equation. This value correlates very well with the primary particle size from TEM images in Fig. 3. Average grain size increased up to 29 nm at 700 °C. Higher temperatures led to further but stronger grain growth and average sizes of 43 nm at 900 °C, 59 nm at 1000 °C and 73 nm at 1100 °C were reached after a dwell time of 3 h in environmental air. The obtained grain sizes after annealing are similar or even smaller if compared to other nanopowder synthesis routines [26]. Nanocrystals (~50 nm) can be kept up to 1000 °C, what offers the possibility for nanostructured electrode layers, but with a significant higher material output as needed for semi-industrial applications. This clearly shows

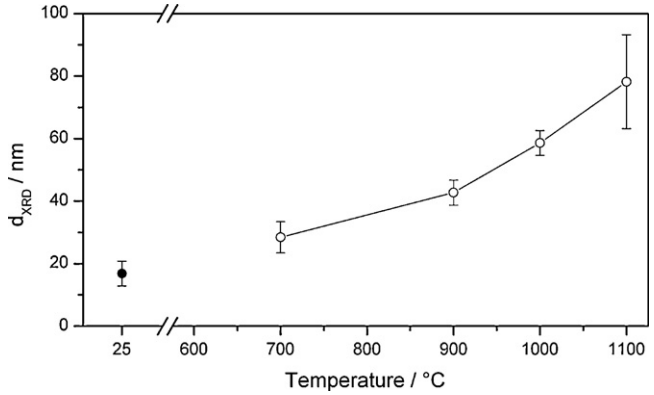

Fig. 6. Average crystal size d_{XRD} as function of annealing temperature with a dwell time of 3 h (○). As-synthesised crystal size is given as reference at 25 °C (●).

the superiority of the FSS process over conventional processing routes.

SEM micrographs of temperature treated powders show, that particle necking led to a fine network at 900 °C but with coexisting larger, spherical particles from the synthesis process (Fig. 7). A homogenous structure with a rather too low open porosity is formed at 1100 °C. From the overall data set it can be assumed that preparation of a porous electrode layer has to be carried out at about 900 °C for the flame-made powders. One the one hand, the $La_{0.6}Sr_{0.4}CoO_{3-\delta}$ powder is phase pure and particle necking is observed, but on the other hand still a nanostructured and fine morphology is obtained and strong particle coarsening is avoided. After thermal treatment between 900 up to 1100 °C and a cooling rate of 5 K min^{-1}, the room temperature derived hexagonal unit cell parameters of flame-made $La_{0.6}Sr_{0.4}CoO_{3-\delta}$ were determined as $a = 5.433$ Å and $c = 13.231$ Å with a resulting unit cell volume

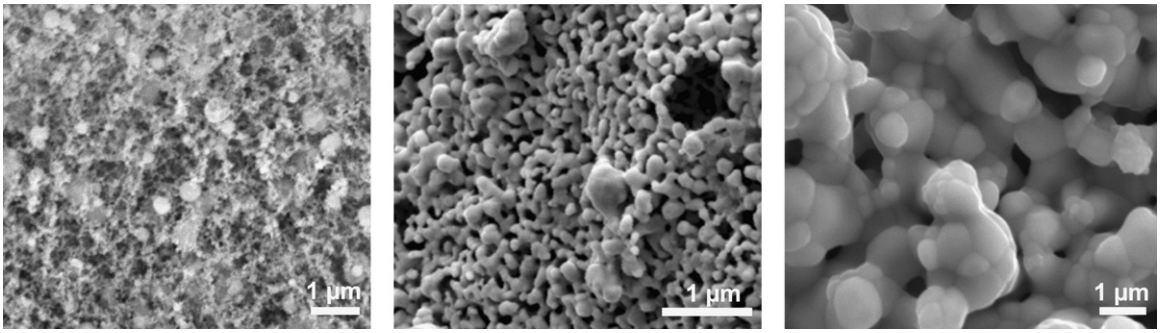

Fig. 7. SEM micrographs from as-synthesised $La_{0.6}Sr_{0.4}CoO_{3-\delta}$ powder (left) and after a dwell time of 3 h at 900 °C (middle) and 1100 °C (right), showing the change in powder morphology and particle size.

Table 1
Thermal expansion coefficient (TEC) of flame-made $La_{0.6}Sr_{0.4}CoO_{3-\delta}$ and common electrolytes compositions applied in an IT-SOFC.

Material composition	TEC/10^{-6} K^{-1} in the temperature range of:			Ref.
	200–650 °C	650–1000 °C	200–1000 °C	
$La_{0.6}Sr_{0.4}CoO_{3-\delta}$	18.0	30.2	22.5	This work
$La_{0.6}Sr_{0.4}CoO_{3-\delta}$	–	–	20.5	[29]
$Y_{0.16}Zr_{0.84}O_2$	11.6	11.6	11.6	[16]
$Sc_{0.20}Ce_{0.01}Zr_{0.79}O_{2-\delta}$	10.6	12.5	11.4	[16]
$Ce_{0.9}Gd_{0.1}O_{2-\delta}$	13.8	15.3	14.4	[16]

of 338.22 Å^3. The application of such powders as screen printing pastes and the later detailed electrochemical and morphological investigation of porous and nanostructured electrode layers are given elsewhere [20,27].

3.3. Electrolyte interaction

Despite the excellent properties of $La_{0.6}Sr_{0.4}CoO_{3-\delta}$ in terms of ionic and electronic conductions [3,28] and its oxygen exchange kinetics [6,29], considerable problems will arise during the processing and/or the later thermal recycling procedure [30]. Layer cracking and delamination takes place at the interface, due to the intrinsic shrinkage behaviour of nanopowders [17,27] as well as to the strong mismatch in the thermal expansion coefficient (TEC) of $La_{0.6}Sr_{0.4}CoO_{3-\delta}$ and that of common electrolytes (Table 1) [30]. To adapt the TEC and to reduce the mechanical stress a certain amount of the electrolyte material is mixed with the cathode powder, from which insulating, because ionic and electronic blocking reaction products ($La_2Zr_2O_7$ and $SrZrO_3$) can be formed during the processing at elevated temperatures [31,32]. Further advantages of such composites are enhanced three-phase-boundary (TPB) length [33,34], better adhesion [35] and suppressed grain growth and coarsening [36]. The focus of our experiments was set on the interesting preparation temperature range of 850–1000 °C, which is applied to the cathode–electrolyte mixture. The here initially created blocking phases reduce the cell performance substantially, while the later lower operation temperature of 600 °C avoids strong material diffusion.

As-synthesised FSS powder with a high specific surface area of 29 m^2 g^{-1} as well as conventional spray pyrolysed and ball-milled $La_{0.6}Sr_{0.4}CoO_{3-\delta}$ powders (9 m^2 g^{-1}) were mixed with three potential low temperature electrolyte compositions to determine their reaction: $Y_{0.16}Zr_{0.84}O_2$ (YSZ) the most common electrolyte and secondly $Sc_{0.20}Ce_{0.01}Zr_{0.79}$ (ScCeZ) was used [37,38]. The latter is a promising electrolyte candidate for an IT-SOFC technology at 600 °C due to its improved conductivity performance. Additionally, $Ce_{0.9}Gd_{0.1}O_{2-\delta}$ (CGO) was used, which is known as a material showing no interaction with $La_{0.6}Sr_{0.4}CoO_{3-\delta}$ and hence widely used as an intermediate layer to prevent secondary phase formation between zirconium, lanthanum and strontium. Cathode and electrolyte powders were mixed in a 1:1 weight ratio in a mortar to guarantee a homogeneous mixture and intimate contact. Diffraction patterns of such pellet mixtures, fired for 4 h at 1000 °C and 125 h at 850 °C are given in Figs. 8–10. A complete overview of formed reaction products and their amounts are given in Table 2.

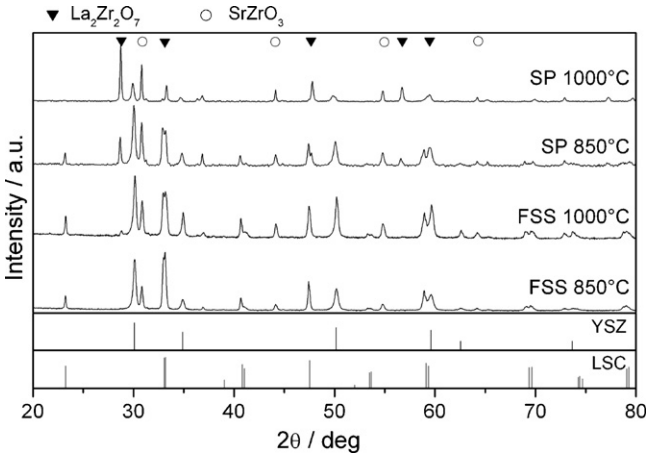

Fig. 8. Diffraction pattern of conventional (SP) and flame-made (FSS) $La_{0.6}Sr_{0.4}CoO_{3-\delta}$ powders fired for 125 h at 850 °C and 4 h at 1000 °C with $Y_{0.16}Zr_{0.84}O_2$. $La_{0.6}Sr_{0.4}CoO_{3-\delta}$ (LSC) and $Y_{0.16}Zr_{0.84}O_2$ (YSZ) are given as reference at the bottom and identified reaction products are marked by the denotation of – ($SrZrO_3$) and ʙ ($La_2Zr_2O_7$).

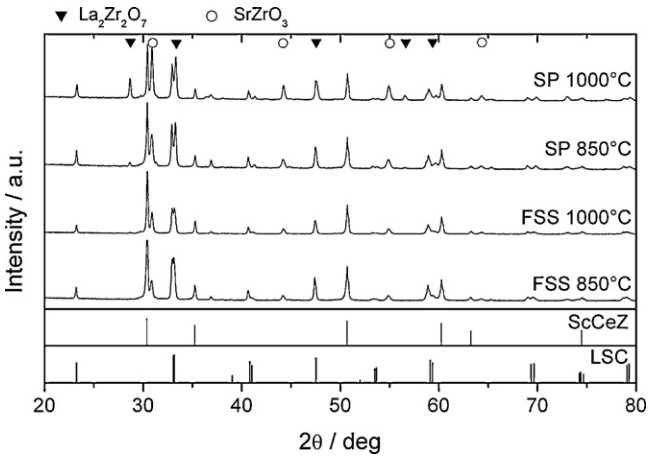

Fig. 9. Diffraction pattern of conventional (SP) and flame-made (FSS) $La_{0.6}Sr_{0.4}CoO_{3-\delta}$ powders fired for 125 h at 850 °C and 4 h at 1000 °C with $Sc_{0.2}Ce_{0.01}Zr_{0.79}O_2$. $La_{0.6}Sr_{0.4}CoO_{3-\delta}$ (LSC) and $Sc_{0.2}Ce_{0.01}Zr_{0.79}O_2$ (ScCeZ) are given as reference at the bottom and identified reaction products are marked by the denotation of – ($SrZrO_3$) and ʙ ($La_2Zr_2O_7$).

Table 2
Weight percentages of $SrZrO_3$ and $La_2Zr_2O_7$ secondary phases calculated from diffraction patterns of 1:1 $La_{0.6}Sr_{0.4}CoO_{3-\delta}$–electrolyte mixtures annealed for 125 h at 850 °C and 4 h at 1000 °C.

Electrolyte	Temperature	FSS made: 29 $m^2\,g^{-1}$ $La_{0.6}Sr_{0.4}CoO_{3-\delta}$		SP made: 9 $m^2\,g^{-1}$ $La_{0.6}Sr_{0.4}CoO_{3-\delta}$	
		$SrZrO_3$	$La_2Zr_2O_7$	$SrZrO_3$	$La_2Zr_2O_7$
YSZ	1000 °C	13%	7%	28%	39%
	850 °C	11%	5%	19%	14%
ScCeZ	1000 °C	12%	3%	27%	12%
	850 °C	8%	1%	17%	6%
CGO	1000 °C	0%	0%	0%	0%
	850 °C	0%	0%	0%	0%

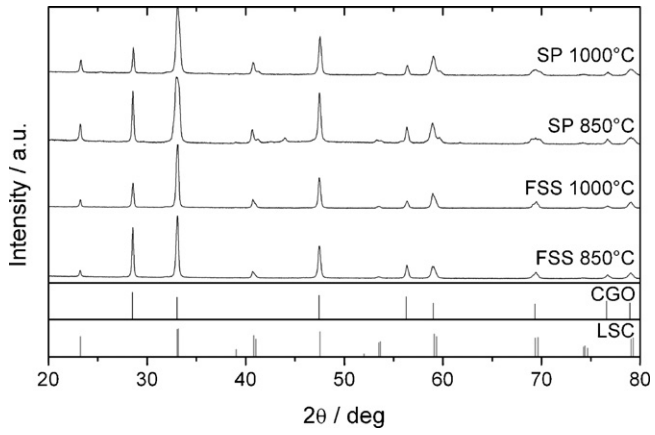

Fig. 10. Diffraction pattern of conventional (SP) and flame-made (FSS) $La_{0.6}Sr_{0.4}CoO_{3-\delta}$ powders fired for 125 h at 850 °C and 4 h at 1000 °C with $Ce_{0.9}Gd_{0.1}O_2$. $La_{0.6}Sr_{0.4}CoO_{3-\delta}$ (LSC) and $Ce_{0.9}Gd_{0.1}O_2$ (CGO) are given as reference at the bottom.

As expected and therefore carried out as a reference, conventional spray pyrolysed, phase pure $La_{0.6}Sr_{0.4}CoO_{3-\delta}$ and YSZ reacted strongly to $SrZrO_3$ (19%) and $La_2Zr_2O_7$ (14%) after 125 h at 850 °C. The overall amount of these phases is even doubled (28% and 39%) when treated for 4 h at 1000 °C and is also observed by many research groups [31,39,40]. The FSS synthesised $La_{0.6}Sr_{0.4}CoO_{3-\delta}$ used in the as-prepared condition and treated in the same way with the same YSZ is showing a significantly lower amount of reaction products, and this in spite of a much higher SSA and expected increased reactivity. At both temperatures the determined amounts were substantially lower, 11% and 5% for $SrZrO_3$ and $La_2Zr_2O_7$, respectively. It is worth to mention, that the flame-made $La_{0.6}Sr_{0.4}CoO_{3-\delta}$ nanopowder is not only less reactive but an increase in the treatment temperature from 850 to 1000 °C did also cause only a marginal increase in the amounts of secondary phases. Especially, if it is compared to the doubling for the conventional spray pyrolysed powder at 1000 °C, where the $La_{0.6}Sr_{0.4}CoO_{3-\delta}$ reflections are nearly completely diminished, e.g. (0 1 2) at 23° or (1 1 0) and (1 0 4) at 33°. The same intensity reduction is observed for the YSZ reflections and supports the strong reaction of the spray pyrolysed $La_{0.6}Sr_{0.4}CoO_{3-\delta}$ powder with YSZ at 1000 °C.

A final explanation for the observed behaviour is difficult to state on basis of the carried out reactivity analysis and further microstructure related elemental analysis will be carried out, but such research is beyond the scope of this work. However, the suppressed reaction for the flame-made powders probably origin from the unique flame conditions: temperatures of about 3000 °C and cooling rates in the order of 500000 $K\,s^{-1}$ conserve high temperature conditions. This kind of flame-made nanopowders in the as-synthesised condition are less crystalline than spray pyrolysis derived powders, since the latter always includes a subsequent firing step to reach the desired phase. In addition, nanopowders exhibit a much higher surface area and hence a larger amount of possible reactive sites. Both properties let one assume a higher reactivity for nanomaterials, but the opposite tendency is observed. It can be presumed at this point, that the unique temperature history causes a non-equilibrated and high temperature related oxygen non-stoichiometry (δ). Furthermore, quenching-related bulk defects [41] as well as defects on the particle surface from the strong curvature of the nanoparticles are created [42,43], which can cause such exceptional behaviour. It is worth to mention here, that flame-made powders often show such exceptional characteristics (cf. Section 3.4). Here, phase analyses of the powders in the as-synthesised condition show that the main perovskite phase can be correlated with the expected hexagonal $La_{0.6}Sr_{0.4}CoO_{3-\delta}$ structure, but the determined unit cell parameters of $a = 5.430$ Å and $c = 13.274$ Å are slightly larger in comparison to the reference (PDF code 01-089-5719). This also indicates a probably non-equilibrated and therefore higher oxygen non-stoichiometry. Some authors proposed a cubic structure, even at room temperature [3,21], but the temperature history and the created defects are here again of high relevance: Petrov et al. also discussed the influence of defects concentration on the formation of perovskite related microdomains with defect ordering, but mentions also clearly that they are not visible by common XRD techniques [3].

Among the substituted zirconates, ScCeZ is one of the most promising electrolyte for an intermediate temperature SOFC technology [37,44]. A higher conductivity than that of YSZ [37,45], minimised phase transition due to absence of a tetragonal phase [46] and hence better long-term stability emphasize this composition as a very promising candidate. The diffraction patterns of both $La_{0.6}Sr_{0.4}CoO_{3-\delta}$ powders in interaction with ScCeZ are shown in Fig. 9 and reaction products are summed up again in Table 2. The formed amounts of reaction products are again substantially lower for the high surface area flame-made powder. About 17% of $SrZrO_3$ and 6% $La_2Zr_2O_7$ were formed at 850 °C from the conventional spray pyrolysed $La_{0.6}Sr_{0.4}CoO_{3-\delta}$, and 27% of $SrZrO_3$ and 12% $La_2Zr_2O_7$ at 1000 °C. In contrast to that, only 8% $SrZrO_3$ and 1% $La_2Zr_2O_7$ at 850 °C, and 12% $SrZrO_3$ and 3% $La_2Zr_2O_7$ at 1000 °C, respectively, were detected by XRD from the flame-made nanopowders. The flame-made $La_{0.6}Sr_{0.4}CoO_{3-\delta}$ powder is again considerably less reactive to this electrolyte material, pointing out that this processing route is resulting in a powder with superior thermal behaviour. Even with a 3 times higher accessible SSA, which offers more reactive sites, less ionic-electronic blocking products are formed. A more general advantage of ScCeZ over YSZ is based on its reduced activity with $La_{0.6}Sr_{0.4}CoO_{3-\delta}$ powders in terms of $La_2Zr_2O_7$ formation. While more or less the same $SrZrO_3$ amounts can be found for the interaction experiments with YSZ and ScCeZ, the $La_2Zr_2O_7$ is not the dominating reaction product anymore. Here, especially the nanoscale flame-made powder is outperforming the conventional powder by 4–5 times lower amounts of $La_2Zr_2O_7$.

To avoid the above-described formation of ionic-electronic blocking compositions of $SrZrO_3$ and $La_2Zr_2O_7$, lower preparation

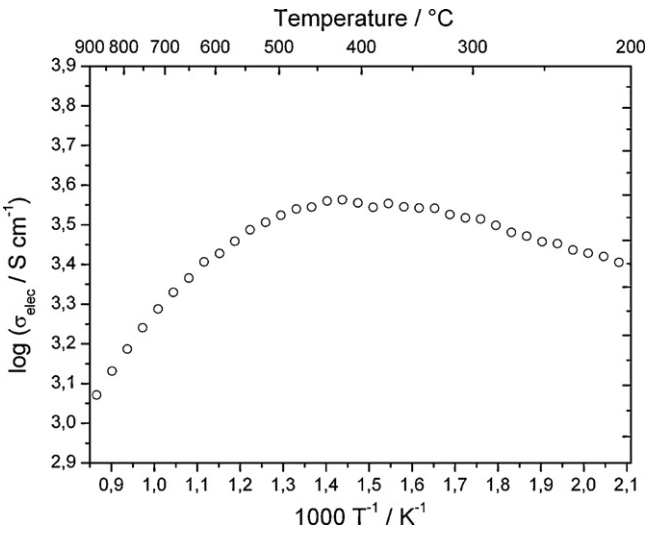

Fig. 11. Electrical conductivity of flame-made $La_{0.6}Sr_{0.4}CoO_{3-\delta}$ as function of temperature in dry synthetic air ($p(O_2) = 0.21$ bar).

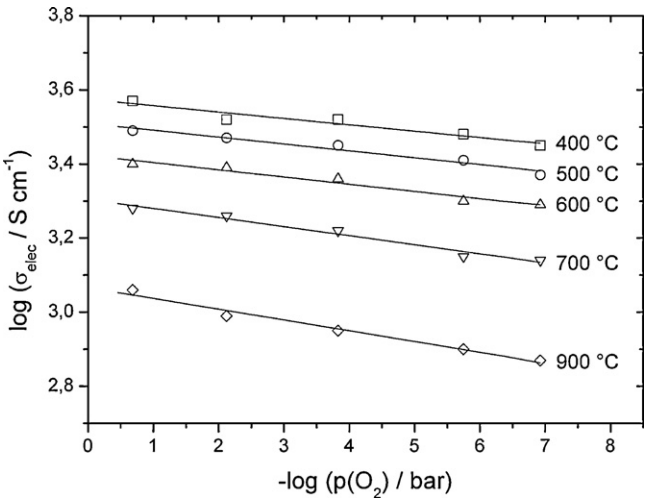

Fig. 12. Electrical conductivity of flame-made $La_{0.6}Sr_{0.4}CoO_{3-\delta}$ as function of the negative logarithm of $p(O_2)$ in the temperature range of 400–900 °C in dry synthetic air.

and operation temperatures have to be applied or a barrier/blocking layer is usually used. CGO is widely applied as a barrier layer and well known as non-reactive to $La_{0.6}Sr_{0.4}CoO_{3-\delta}$ [47–49]. As expected, both powders showed independent of particle size, phase purity or synthesis route no secondary phases or a shift in the diffraction patterns (Fig. 10 and Table 2). Such a barrier layer of CGO is highly needed even for IT-SOFCs, as long as cell preparation temperatures are in the investigated high temperature range of 850–1000 °C.

3.4. Bulk conductivity properties

Electrical bulk conductivity and $p(O_2)$ dependency at various temperatures were characterised by four-point DC method on the cooling branch (1 K min^{-1}). The electrical bulk conductivity in dry air reached its maximum with 3600 S cm^{-1} at 400 °C and decreased then over 2680 S cm^{-1} at 600 °C to 1150 S cm^{-1} at 900 °C (Fig. 11). This reflects the expected metallic-like conductivity and the decrease in the electron-hole concentration with increasing temperature. At the aimed operating temperature of about 600 °C, the observed electrical conductivity of the flame-made $La_{0.4}Sr_{0.6}CoO_{3-\delta}$ is considerable higher than the 2000 S cm^{-1} reported by various groups [30,50], but even lower values of 1400 down to 800 S cm^{-1} are reported [5,51]. Within this temperature range of 400–900 °C electrical conductivity is determined as function of oxygen partial pressure $p(O_2)$, which changes along the cathode thickness during operation: from air (0.21 bar = 2.1×10^5 Pa) down to 0.12 ppm (1.2×10^{-7} bar = 1.2×10^{-2} Pa) (Fig. 12). A constant but weak linear slope over the whole $p(O_2)$ range is observed in the $\log \sigma - \log p(O_2)$ plot. With a temperature increase from 400 to 900 °C the $p(O_2)$ dependence gets stronger: a dependency of −0.017 is determined at 400 °C which increases progressively to −0.023 at 600 °C and −0.029 at 900 °C. This results from an increase of δ, caused by the reduction of oxygen vacancies with temperature and is consistent to Mizusaki et al. [52]. Further on, the absence of any plateau or inflection point in the investigated temperature range indicates a metallic behaviour and that electrons are not localised to the Co ions [52,53].

One should note that at temperatures below 400 °C electric bulk conductivity decreases again towards room temperature. Such semiconductor-like temperature dependence is usually observed for Sr contents of $x < 0.4$ in $La_{1-x}Sr_xCoO_{3-\delta}$, although Mizusaki et al. [54] also found a change from metallic to semiconductor behaviour in the range of $0.3 < x < 0.5$, but with a less pronounced maximum in the electrical conductivity at about 300 °C. Also Bucher et al. [55] found a positive activation energy for larger δ under low oxygen contents in $La_{0.4}Sr_{0.6}CoO_{3-\delta}$. This metal–insulator (M–I) transition is related to changes in Co–O distance and Co–O–Co angle [56] and is strongly influenced by oxygen vacancies, strontium (hole) doping or operation temperature and all of them are affecting this transition. Mineshige et al. [57] found a change from metallic to semiconductor behaviour as function of the quenching rate of a $La_{0.7}Sr_{0.3}CoO_{3-\delta}$ sample, which was explained by a conserved oxygen non-stoichiometry condition and by annealing at lower $p(O_2)$.

This leads again to the assumption that a high temperature condition (>3000 °C) in terms of a higher oxygen non-stoichiometry (δ) and additional defects are preserved in the flame-made material by the huge quenching rates (>500000 K s^{-1}). This results in a lattice distortion and the observed larger unit cell parameters in this work. This would also explain the wide range of observed materials properties in literature (electrical conductivity, oxygen deficiency or M–I transition) due to the substantially different processing conditions, e.g. cooling rate, calcination temperature and dwell time [30,50,56]. Some literature even refers to samples prepared at 1390 °C [30], where the here presented flame-made material shows a very strong decomposition and do not reflect the $La_{0.6}Sr_{0.4}CoO_{3-\delta}$ characteristics anymore (Fig. 5). However, deviations in the phase composition can be excluded from our XRD measurements, and hence we can attribute the observed electrical characteristics to the particular synthesis routine. Additionally it is well known, that flame-derived materials, synthesised at such high temperatures with the subsequent strong quenching, often show outstanding properties, i.e. significant higher doping and substitution levels compared to conventional solid state preparation methods [41,58,59], emphasised conductivity properties as it is observed in this work as well as better homogeneity in the elemental distribution in the crystals [17].

3.5. Symmetrical cell measurement and CO_2 sensitivity

Fig. 13 shows the area specific resistance (ASR) as function of temperature of screen printed symmetrical $La_{0.6}Sr_{0.4}CoO_{3-\delta}$ electrodes prepared at 900 °C on a 1.5 mm thick $Ce_{0.9}Gd_{0.1}O_2$ elec-

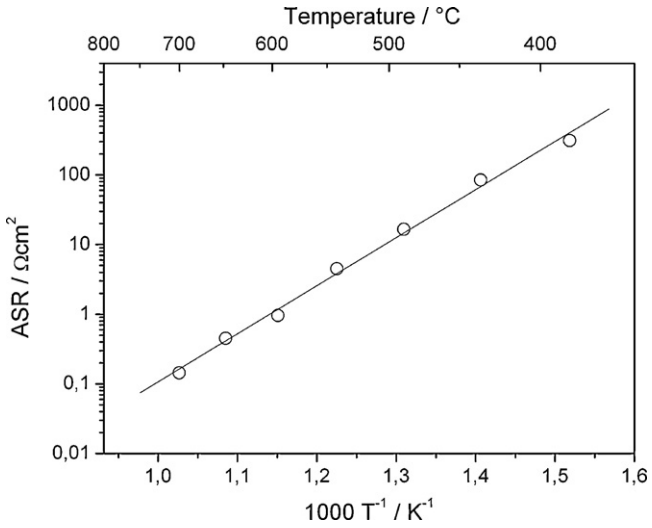

Fig. 13. Temperature dependence of ASR for screen printed $La_{0.6}Sr_{0.4}CoO_{3-\delta}$ nanopowder prepared at 900 °C on a $Ce_{0.9}Gd_{0.1}O_{2-\delta}$ substrate in air.

trolyte. An ASR of 0.96 Ω cm^2 at 600 °C and 0.14 Ω cm^2 at 700 °C are encouraging and promising results, keeping in mind that this is a relatively dense and non-optimised microstructure (cf. Fig. 7). Tao et al. [50] reported minimal higher ASR of 0.17 Ω cm^2 at 700 °C, but a significant lower conductivity (see Section 3.4) for the same annealing temperature. Nevertheless, they reported comparable values for a nanostructured $La_{0.4}Sr_{0.6}CoO_{3-\delta}$ cathode by a complexing method, although it has to be stated clearly, that this synthesis has to deal with the drawback of upscaling, while the here presented process can provide up to 400 g h^{-1} [17].

It is expected that a more open porous structure performs better due to an optimised gas distribution in the electrode. An extensive microstructure investigation as well as a strategy towards a further improvement and its influence on the electrochemical performance of this flame-derived powder is given elsewhere [27]. Due to their outstanding shrinkage behaviour, it has to be clearly stated at this point, that the control over microstructure seems to be the most important factor during electrode layer processing via screen printing of nanopowders [20].

During long-term operation at 600 °C, typical CO_2 concentrations of 385 ppm in air in combination with an accessible high specific surface area can cause carbonate formation from the high amount of strontium, similar to the carbonate formation of barium containing cathode materials [17,60]. For this reason CO_2 sensitivity of nanoscale $La_{0.6}Sr_{0.4}CoO_{3-\delta}$ powder was investigated by TGA of powders and by long-term conductivity measurements in 5% CO_2 containing atmosphere.

TGA in dry and CO_2-free synthetic air shows progressive loss of weight from room temperature (RT) to 900 °C on, indicating the ongoing oxygen loss and increasing δ in $La_{0.6}Sr_{0.4}CoO_{3-\delta}$ (Fig. 14). A slightly lower mass loss is observed in 5% CO_2 in air, probably due to a reduced oxygen exchange kinetic caused by the CO_2 [60], but no indicator for carbonate formation was found. No mass uptake can be observed at all, what means that no formation of electronic blocking $SrCO_3$ takes place under the investigated conditions. This is supported by measured electrical bulk resistivity under same atmospheric conditions in Fig. 15. Reference bulk resistivity was measured for an initial phase of 48 h in CO_2-free dry synthetic air at 600 °C to obtain a stable reference conductivity value. To decouple possible strontium hydroxide caused effects [61], gas composition was switched from dry, CO_2-free synthetic air to a dry, CO_2-rich atmosphere with 5% CO_2. Within the next 132 h a marginal change of -3.7×10^{-7} Ω cm per 24 h (−0.1% per 24 h) was observed, what

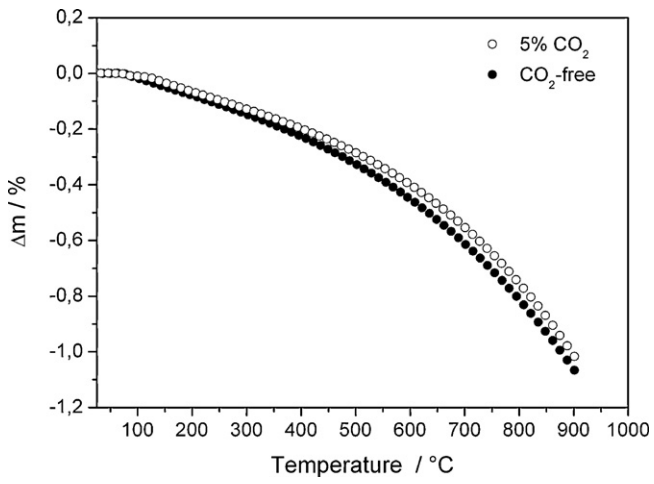

Fig. 14. Thermo-gravimetric analysis of flame-derived powder in CO_2-free dry synthetic air and in dry synthetic air with 5% CO_2 (heating rate: 1 K min^{-1}).

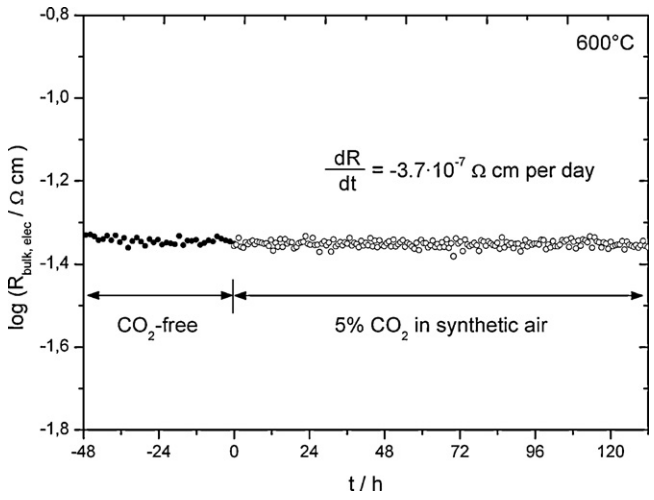

Fig. 15. Electrical bulk resistivity of $La_{0.6}Sr_{0.4}CoO_{3-\delta}$ as function of time at 600 °C in CO_2-free and 5% CO_2 in dry synthetic air.

is interpreted as a stable operation. $La_{0.6}Sr_{0.4}CoO_{3-\delta}$ seems to be non-sensitive towards CO_2 uptake and the formation of any carbonate phase at 600 °C, even at such high CO_2 concentrations of about 5%.

4. Conclusion

Flame spray synthesis (FSS) technology was used to synthesise nanoscale $La_{0.6}Sr_{0.4}CoO_{3-\delta}$ powder with a specific surface area of 29 m^2 g^{-1} at industrial relevant large-scale production scale of 135 g h^{-1}. Cost-effective nitrates were used as precursor and dissolved in a water-based solvent with 30 vol.% of acetic acid. These conditions were identified as an optimum for the suppression of secondary $(La,Sr)_2CoO_4$ phase formation as well as this improved the homogeneity of the power.

Although not phase pure in the as-synthesised condition, phase purity can be obtained at temperatures between 800 and 900 °C and nanocrystallinity (~50 nm) can be conserved up to 1000 °C. A remarkable characteristic of the flame-made $La_{0.6}Sr_{0.4}CoO_{3-\delta}$ powder was revealed by electrolyte interaction experiments. The flame-made, nanoscale $La_{0.6}Sr_{0.4}CoO_{3-\delta}$ in the as-synthesised and non-phase pure condition showed a significantly lower reactivity with $Y_{0.16}Zr_{0.84}O_{2-\delta}$ and $Sc_{0.20}Ce_{0.01}Zr_{0.79}O_{2-\delta}$ if compared to conventional spray pyrolysed $La_{0.6}Sr_{0.4}CoO_{3-\delta}$ of about 9 m^2 g^{-1}. An up

to 6 times lower amount of $La_2Zr_2O_7$ and 2 times lower amount of $SrZrO_3$ were detected for the flame-made $La_{0.6}Sr_{0.4}CoO_{3-\delta}$, in spite of its high surface area and hence more contact sites.

TGA (25–900 °C) and long-term conductivity measurements (600 °C) gave no evidence for a tendency to form carbonates from $La_{0.6}Sr_{0.4}CoO_{3-\delta}$, even in 5% CO_2 containing atmosphere.

Screen printed cathode layers were sintered at 900 °C and resulted in relatively dense and nanoporous layers but with good electrochemical performance at intermediate temperatures. ASR values of 0.96 Ω cm^2 at 600 °C and 0.14 Ω cm^2 at 700 °C were obtained in air from symmetrical cells on base of a $Ce_{0.9}Gd_{0.1}O_{2-\delta}$ electrolyte. Conductivity as high as 2680 S cm^{-1} at 600 °C and rather semiconductor-like behaviour were observed, probably caused by a anomalous oxygen non-stoichiometry or defect-related distortions related to the outstanding flame synthesis conditions, namely very high synthesis temperatures about 3000 °C and extreme quenching rates of 500000 K s^{-1}. Against the background of the morphological observations, it is believed to further increase the performance of the nanostructured $La_{0.6}Sr_{0.4}CoO_{3-\delta}$ layers by improving porosity or using $La_{0.4}Sr_{0.6}CoO_{3-\delta}/Ce_{0.9}Gd_{0.1}O_{2-\delta}$ composite, to consider the TEC mismatch and to enhance the three-phase-boundary length.

Acknowledgements

The authors gratefully acknowledge the funding provided by the EC in the framework of the integrated project SOFC600 (SES6 2006020089) and the scientific discussions with the project partners. Thanks to Nikolaos Karageorgakis and Lorenz Holzer (EMPA) for their intensive engagement and assistance during the project work.

References

[1] Y. Zhang-Steenwinkel, M.M.A. van Tuel, F.P.F. van Berkel, G. Rietveld, in: K. Eguchi, S.C. Singhai, H. Yokokawa, H. Mizusaki (Eds.), Solid Oxide Fuel Cells 10, vol. 7, 2007, pp. 271–278.
[2] Demonstration of SOFC stack technology for operation at 600 °C (SOFC600/SES6-2006020089) can be found under www.sofc600.eu, 2009.
[3] A.N. Petrov, O.F. Kononchuk, A.V. Andreev, V.A. Cherepanov, P. Kofstad, Solid State Ionics 80 (1995) 189–199.
[4] A.N. Petrov, V.A. Cherepanov, A.Y. Zuev, J. Solid State Electrochem. 10 (2006) 517–537.
[5] A. Weber, Doctoral Thesis, University of Karlsruhe, Germany, 2002.
[6] S.B. Adler, Solid State Ionics 111 (1998) 125–134.
[7] L.M. van der Haar, M.W. den Otter, M. Morskate, H.J.M. Bouwmeester, H. Verweij, J. Electrochem. Soc. 149 (2002) J41–J46.
[8] L. Dieterle, D. Bach, R. Schneider, H. Störmer, D. Gerthsen, U. Guntow, E. Ivers-Tiffée, A. Weber, C. Peters, H. Yokokawa, J. Mater. Sci. 43 (2008) 3135–3143.
[9] M. Sase, J. Suzuki, K. Yashiro, T. Otake, A. Kaimai, T. Kawada, J. Mizusaki, H. Yugami, Presented at 15th International Conference on Solid State Ionics, Baden Baden, Germany, 2006.
[10] H.L. Tuller, Solid State Ionics 131 (2000) 143–157.
[11] A. Endo, H. Fukunaga, C. Wen, K. Yamada, Presented at 12th International Conference on Solid State Ionics, Halkidiki, Greece, June 06–12, 1999.
[12] N.P. Bansal, Z. Zhong, J. Power Sources 158 (2006) 148–153.
[13] F. Zhao, R. Peng, C. Xia, Fuel Cells Bull. 2008 (2008) 12–16.
[14] J. Januschewsky, M. Ahrens, A. Opitz, F. Kubel, J. Fleig, Adv. Funct. Mater. 19 (2009) 3151–3156.
[15] D.O. Klenov, W. Donner, L. Chen, A.J. Jacobson, S. Stemmer, J. Mater. Res. 18 (2003) 188–194.
[16] A. Heel, A. Vital, P. Holtappels, T. Graule, J. Electroceram. 22 (2009) 40–46.
[17] A. Heel, P. Holtappels, P. Hug, T. Graule, Fuel Cells, in press, doi:fuce.200900093.
[18] A.L. Patterson, Phys. Rev. 56 (1939) 978.
[19] P. Scherrer, Nachr K. Ges. Wiss. Goettingen, Math. Phys. Kl 2 (1918) 98–100.
[20] D. Burnat, P. Ried, P. Holtappels, A. Heel, T. Graule, D. Kata, 10 (2009) 156–165.
[21] R. Sonntag, S. Neov, V. Kozhukharov, D. Neov, J.E. ten Elshof, Phys. B: Condens. Mat. 241–243 (1997) 393–396.
[22] G. Demazeau, P. Courbin, G.L. Flem, M. Pouchard, P. Hagenmuller, J.L. Soubeyroux, I.G. Main, G.A. Robins, New J. Chem. 3 (1979) 171–174.
[23] G.L. Messing, S.C. Zhang, G.V. Jayanthi, J. Am. Ceram. Soc. 76 (1993) 2707–2726.
[24] W.C. Hinds, Aerosol Technology, John Wiley & Sons, New York, 1999.
[25] R. Jossen, R. Mueller, S.E. Pratsinis, M. Watson, M.K. Akhtar, Nanotechnology 16 (2005) S609–S617.
[26] J.X. Wang, Y.K. Tao, J. Shao, W.G. Wang, J. Power Sources 186 (2009) 344–348.
[27] M. Prestat, A. Morandi, A. Heel, L. Holzer, P. Holtappels, T.J. Graule, Electrochem. Commun. 12 (2010) 292–295.
[28] K. Huang, H.Y. Lee, J.B. Goodenough, J. Electrochem. Soc. 145 (1998) 3220–3227.
[29] K. Huang, J.B. Goodenough, J. Electrochem. Soc. 148 (2001) E203–E214.
[30] A. Petric, P. Huang, F. Tietz, Solid State Ionics 135 (2000) 719–725.
[31] O. Yamamoto, Y. Takeda, R. Kanno, M. Noda, Solid State Ionics 22 (1987) 241–246.
[32] M. Sase, D. Ueno, K. Yashiro, A. Kaimai, T. Kawada, J. Mizusaki, Presented at 11th International Conference on High Temperature Materials Chemistry (HTMC-XI), Tokyo, Japan, May 19–23, 2003.
[33] M. Mogensen, S. Skaarup, Solid State Ionics 86–88 (1996) 1151–1160.
[34] J. Mizusaki, H. Tagawa, K. Tsuneyoshi, A. Sawata, J. Electrochem. Soc. 138 (1991) 1867–1873.
[35] X.D. Zhu, K.N. Sun, N.Q. Zhang, X.B. Chen, L.J. Wu, D.C. Jia, Electrochem. Commun. 9 (2007) 431–435.
[36] M.R. Nateghi, M.R. Barzegari, J. Alloys Compd. 452 (2008) 36–40.
[37] A. Smirnova, V. Sadykov, V. Muzykantov, N. Mezentseva, V. Ivanov, V. Zaikovskii, A. Ishchenko, N. Sammes, O. Vasylyev, J. Kilner, J. Irvine, V. Vereschak, I. Kosacki, N. Uvarov, V. Zyryanov, Mater. Res. Soc. Symp. Proc. 972 (2007).
[38] Z. Wang, M. Cheng, Y. Dong, M. Zhang, H. Zhang, J. Power Sources 156 (2006) 306–310.
[39] H. Yokokawa, N. Sakai, T. Kawada, M. Dokiya, Solid State Ionics 40–41 (1990) 398–401.
[40] H.Y. Tu, Y. Takeda, N. Imanishi, O. Yamamoto, Solid State Ionics 117 (1999) 277–281.
[41] M. Radecka, M. Rekas, E. Kusior, K. Zakrzewska, A. Heel, K.A. Michalow, T. Graule, J. Nanosci. Nanotechnol. 10 (2010) 1032–1042.
[42] K.A. Michalow, A. Vital, A. Heel, T. Graule, F.A. Reifler, A. Ritter, K. Zakrzewska, M. Rekas, J. Adv. Oxid. Technol. 11 (2008) 56–64.
[43] M. Casas-Cabanas, G. Binotto, D. Larcher, A. Lecup, V. Giordani, J.M. Tarascon, Chem. Mater. 21 (2009) 1939–1947.
[44] Z. Wang, M. Cheng, Z. Bi, Y. Dong, H. Zhang, J. Zhang, Z. Feng, C. Li, Mater. Lett. 59 (2005) 2579–2582.
[45] D. Lee, I. Lee, Y. Jeon, R. Song, Solid State Ionics 176 (2005) 1021–1025.
[46] S.P.S. Badwal, F.T. Ciacchi, D. Milosevic, Solid State Ionics 136–137 (2000) 91–99.
[47] A. Mai, V.A.C. Haanappel, F. Tietz, D. Stöver, Solid State Ionics 177 (2006) 2103–2107.
[48] H. Uchida, S. Arisaka, M. Watanabe, Electrochem. Solid State Lett. 2 (1999) 428–430.
[49] A. Tsoga, A. Gupta, A. Naoumidis, P. Nikolopoulos, Acta Mater. 48 (2000) 4709–4714.
[50] Y. Tao, J. Shao, J. Wang, W.G. Wang, J. Power Sources 185 (2008) 609–614.
[51] Y. Teraoka, H.M. Zhang, K. Okamoto, N. Yamazoe, Mater. Res. Bull. 23 (1988) 51–58.
[52] J. Mizusaki, Y. Mima, S. Yamauchi, K. Fueki, H. Tagawa, J. Solid State Chem. 80 (1989) 102–111.
[53] S.B. Adler, Chem. Rev. 104 (2004) 4791–4844.
[54] J. Mizusaki, J. Tabuchi, T. Matsuura, S. Yamauchi, K. Fueki, J. Electrochem. Soc. 136 (1989) 2082–2088.
[55] E. Bucher, W. Jantscher, A. Benisek, W. Sitte, W. Preis, I. Rom, F. Hofer, Solid State Ionics 141–142 (2001) 375–380.
[56] A. Mineshige, M. Inaba, T.S. Yao, Z. Ogumi, K. Kikuchi, M. Kawase, J. Solid State Chem. 121 (1996) 423–429.
[57] A. Mineshige, M. Kobune, S. Fujii, Z. Ogumi, M. Inaba, T. Yao, K. Kikuchi, J. Solid State Chem. 142 (1999) 374–381.
[58] A. Trenczek-Zajac, M. Radecka, M. Jasinski, K.A. Michalow, M. Rekas, E. Kusior, K. Zakrzewska, A. Heel, T. Graule, K. Kowalski, J. Power Sources 194 (2009) 104–111.
[59] W.Y. Teoh, R. Amal, L. Madler, S.E. Pratsinis, Catal. Today 120 (2007) 203–213.
[60] E. Bucher, A. Egger, G.B. Caraman, W. Sitte, J. Electrochem. Soc. 155 (2008) B1218–B1224.
[61] P. Hjalmarsson, M. Søgaard, M. Mogensen, Solid State Ionics 179 (2008) 1422–1426.